

Next-Generation Grid Codes: Toward a New Paradigm for Dynamic Ancillary Services

Verena Häberle[†], Kehao Zhuang[‡], Xiuqiang He[§], Linbin Huang[‡], Florian Dörfler[†]

Abstract—This paper presents *preliminary results toward a conceptual foundation for Next Generation Grid Codes (NGGCs) based on decentralized stability and performance certification for dynamic ancillary services*. The proposed NGGC framework targets two core outcomes: (i) guaranteed closed-loop stability and (ii) explicit performance assurances for power-system frequency and voltage dynamics. Stability is addressed using loop-shifting and passivity-based methods that yield local frequency-domain certificates for individual devices, enabling fully decentralized verification of the interconnected system. Performance is characterized by deriving quantitative bounds on key time-domain metrics (e.g., nadirs, rate-of-change-of-frequency (RoCoF), steady-state deviations, and oscillation damping) through frequency-domain constraints on local device behavior. The framework is non-parametric and model-agnostic, accommodating a broad class of device dynamics under mild assumptions, and provides an initial unified approach to stability and performance certification without explicit device-model parameterization. As such, these results offer a principled starting point for the development of future grid codes and control design methodologies in modern power systems.

I. INTRODUCTION

Current grid codes for dynamic ancillary services with converter-based generation, such as fast frequency and voltage regulation, are predominantly specified through prescribed time-domain step responses and response-time limits. The European network code [1], for instance, defines frequency containment and voltage regulation via piecewise-linear active and reactive power curves, while national codes in Finland [2] and Germany [3] similarly prescribe fast frequency reserves and synthetic inertia using power injection profiles or time constants. Although conceptually simple, these requirements are often implemented through open-loop commands or look-up tables, resulting in rigid and inefficient control. Moreover, existing codes focus mainly on grid-following operation, with only recent exceptions of including grid-forming requirements [3], and they offer no guarantees of closed-loop stability or system performance. As a result, systems that comply with current grid codes may still exhibit poor dynamic behavior or instability [4], [5].

Recent grid-code proposals [6] have begun to address closed-loop stability and performance guarantees using frequency-domain concepts. However, their scope remains limited to single-device-to-grid connections and qualitative disturbance rejection, without providing explicit bounds on key metrics such as frequency nadir or RoCoF. Related efforts to incorporate passivity requirements into grid-forming control design [7] face similar challenges, as power system networks are not inherently passive. These limitations motivate the need for a more general,

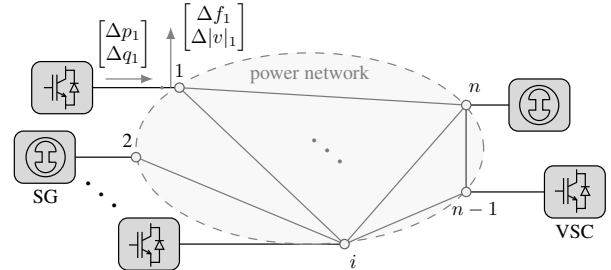


Fig. 1: Multi-device transmission system with SGs and grid-forming VSCs connected by resistive-inductive transmission lines.

quantitative, and practically implementable framework to specify dynamic ancillary services in future grid codes.

This paper introduces the concept of *Next Generation Grid Codes (NGGCs)* as a first step toward a new paradigm for dynamic ancillary services based on decentralized frequency-domain criteria. The NGGC framework provides two main benefits: (i) guaranteed closed-loop stability and (ii) explicit performance guarantees at the system level. For stability, we employ loop-shifting and passivity-based techniques to derive decentralized certificates that translate into local tuning rules for individual devices, ensuring modular contributions to global stability. For performance, we establish quantitative bounds on critical time-domain indicators of small-signal frequency and voltage dynamics, including frequency and voltage nadirs, RoCoF, steady-state deviations, and oscillation damping. These bounds are obtained by linking time-domain metrics to frequency-domain constraints on local device behavior and can be expressed as Nyquist-plot envelopes on device transfer functions. The framework naturally accommodates grid-forming signal causality and integrates with existing converter and synchronous-generator models.

Unlike existing decentralized stability certification methods that rely on explicit device parameterizations [4], [8], [9], the proposed approach is model-agnostic and applies to heterogeneous devices under mild behavioral assumptions. While related generic certificates based on small-gain, small-phase, or sector conditions have been reported [10], [11], the present work extends these results by simultaneously providing explicit stability and performance guarantees. To the best of our knowledge, this is the first unified framework that ensures both closed-loop stability and quantitative performance bounds for frequency and voltage dynamics under general, non-parametric device models.

II. POWER SYSTEM MODEL

Small-Signal Network Dynamics: We consider an interconnected power system composed of three-phase generation units, including grid-forming voltage-source converters (VSCs) and synchronous generators (SGs), connected through a balanced resistive-inductive transmission network. The network is represented in Kron-reduced form with n generator buses, as illustrated in Fig. 1.

[†]Verena Häberle and Florian Dörfler are with the Automatic Control Laboratory, ETH Zurich, 8092 Zurich, Switzerland. Email: {verenahae,dorfler}@ethz.ch

[‡] Kehao Zhuang and Linbin Huang are with the College of Electrical Engineering, Zhejiang University, Hangzhou 310027, China. Email: {hlinbin,zhuangkh}@zju.edu.cn

[§] Xiuqiang He is with the Department of Automation, Tsinghua University, Beijing 100084, China. Email: hxq19@tsinghua.org.cn

The network dynamics are modeled using a quasi-stationary small-signal representation in the global per-unit system, which relates deviations in bus frequencies $\Delta f = [\Delta f_1 \dots \Delta f_n]^\top$ and voltage magnitudes $\Delta|v| = [\Delta|v|_1 \dots \Delta|v|_n]^\top$ to the corresponding active and reactive power injections $\Delta p = [\Delta p_1 \dots \Delta p_n]^\top$ and $\Delta q = [\Delta q_1 \dots \Delta q_n]^\top$. Specifically, the transmission network is described by a $2n \times 2n$ transfer matrix $N(s)$ (see [9] for a detailed derivation), such that

$$\begin{bmatrix} \Delta p(s) \\ \Delta q(s) \end{bmatrix} = \underbrace{\begin{bmatrix} N^{\text{fp}}(s) & 0 \\ 0 & N^{\text{qv}} \end{bmatrix}}_{=: N(s)} \begin{bmatrix} \Delta f(s) \\ \Delta|v|(s) \end{bmatrix}, \quad (1)$$

revealing a decoupling between the active-power-frequency (pf) and reactive-power-voltage (qv) dynamics. The pf-coupling is captured by the $n \times n$ matrix $N^{\text{fp}}(s)$ with entries

$$\begin{aligned} N_{ii}^{\text{fp}}(s) &= \frac{1}{s} \frac{2\pi}{1+\rho^2} \sum_{j \neq i}^n b_{ij} |v|_{0,i} |v|_{0,j}, \\ N_{ij}^{\text{fp}}(s) &= -\frac{1}{s} \frac{2\pi}{1+\rho^2} b_{ij} |v|_{0,i} |v|_{0,j}, \end{aligned} \quad (2)$$

while the qv-coupling is described by the static $n \times n$ matrix N^{qv} with elements

$$\begin{aligned} N_{ii}^{\text{qv}} &= \frac{1}{1+\rho^2} \sum_{j \neq i}^n b_{ij} (2|v|_{0,i} - |v|_{0,j}), \\ N_{ij}^{\text{qv}} &= -\frac{1}{1+\rho^2} b_{ij} |v|_{0,i}. \end{aligned} \quad (3)$$

Here, $|v|_{0,i}$ denotes the steady-state voltage magnitude at node i , $b_{ij} = 1/l_{ij}$ is the line susceptance, and $\rho_{ij} = r_{ij}/l_{ij}$ is the resistance-to-inductance ratio of line ij . The network is assumed to be dominantly inductive, with a small and uniform $\rho_{ij} = \rho \ll 1$. If no line connects nodes i and j , we set $b_{ij} = \rho_{ij} = 0$.

Small-Signal Device Dynamics: We model generation units with grid-forming signal causality, i.e., devices that regulate frequency and voltage outputs based on measured active and reactive power deviations. The linearized dynamics of the i -th device are described by a diagonal 2×2 transfer matrix

$$\begin{bmatrix} \Delta f_i(s) \\ \Delta|v|_i(s) \end{bmatrix} = \begin{bmatrix} D_i^{\text{pf}}(s) & 0 \\ 0 & D_i^{\text{qv}}(s) \end{bmatrix} \begin{bmatrix} \Delta p_i(s) \\ \Delta q_i(s) \end{bmatrix}. \quad (4)$$

The device dynamics $D_i^{\text{pf}}(s)$ and $D_i^{\text{qv}}(s)$ allow for arbitrary rational transfer functions that capture decoupled pf- and qv-behavior. This model-agnostic representation accommodates a wide range of devices, including grid-forming VSCs and SGs, without relying on explicit parameterizations. Stacking all device models yields the overall device dynamics, i.e.,

$$\begin{bmatrix} \Delta f(s) \\ \Delta|v|(s) \end{bmatrix} = \underbrace{\begin{bmatrix} D^{\text{pf}}(s) & 0 \\ 0 & D^{\text{qv}}(s) \end{bmatrix}}_{=: D(s)} \begin{bmatrix} \Delta p(s) \\ \Delta q(s) \end{bmatrix} \quad (5)$$

where $D^{\text{pf}}(s) = \text{diag}(D_i^{\text{pf}}(s))$ and $D^{\text{qv}}(s) = \text{diag}(D_i^{\text{qv}}(s))$.

Interconnected Power System: The closed-loop power system is modeled as the feedback interconnection of the device dynamics (5) and the network dynamics (1), denoted by $D \# N$ (Fig. 2a). Due to the decoupling of device and network dynamics, this interconnection separates into pf- and qv-subsystems.

For stability analysis, we retain the full multi-node feedback interconnection to capture inter-node coupling. For performance analysis, we adopt reduced representations consistent with grid-code practice, namely the average-mode system frequency response of the pf-subsystem, and local voltage responses of

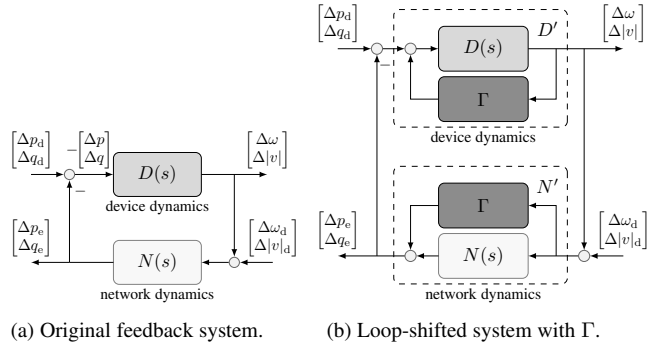


Fig. 2: Closed-loop power system with active and reactive power disturbances Δp_d and Δq_d , and frequency and voltage disturbances Δf_d and $\Delta|v|_d$.

the qv-subsystem. This enables the derivation of decentralized conditions on each $D_i^{\text{pf}}(s)$ and $D_i^{\text{qv}}(s)$, ensuring both closed-loop stability and performance of the overall power system.

Average-Mode System Frequency: Assuming stability of the pf-subsystem, the closed-loop mapping from active-power disturbances to frequency deviations is characterized by the network Laplacian. Its eigenvalue decomposition reveals that the dominant low-frequency behavior is governed by the coherent (average-mode) system frequency response [12], i.e.,

$$\Delta f_{\text{avg}}(s) \approx \underbrace{\left(\sum_{i=1}^n \left(D_i^{\text{pf}}(s) \right)^{-1} \right)^{-1}}_{=: D_{\text{avg}}(s)} \underbrace{\sum_{i=1}^n \Delta p_{d,i}(s)}_{=: \Delta p_d^{\Sigma}(s)}. \quad (6)$$

III. DEVICE-LEVEL CERTIFICATION METHODS

A. Stability Certification Criteria

By applying loop-shifting and passivity-based arguments as in [9], we derive decentralized, device-level conditions that ensure internal feedback stability of the closed-loop interconnection $D \# N$. In particular, since the network transfer matrix $N(s)$ is not inherently passive, we introduce a block-diagonal loop-shifting matrix $\Gamma = \text{diag}(0_{n \times n}, \Gamma^{\text{qv}})$, leading to the loop-shifted interconnection $D' \# N'$ in Fig. 2b. The $n \times n$ matrix

$$\Gamma^{\text{qv}} = \text{diag}(c_i), \quad c_i = \sum_{j \neq i}^n b_{ij} \frac{0.8}{1+\rho^2}, \quad (7)$$

is selected such that the loop-shifted network $N'(s)$ is passive [9]. The corresponding loop-shifted device dynamics $D'(s)$ are

$$D'(s) = \begin{bmatrix} D^{\text{pf}}(s) & 0 \\ 0 & D^{\text{qv}}(s)(I - \Gamma^{\text{qv}} D^{\text{qv}}(s))^{-1} \end{bmatrix} \quad (8)$$

Internal stability of $D' \# N'$ (and hence $D \# N$) follows if $D'(s)$ is strictly passive and a mild small-gain condition at $\omega = \infty$ holds [9]. Because (8) is diagonal, the conditions separate into independent constraints for the pf- and qv-channels.

Frequency control: Strict passivity and the small-gain condition of $D^{\text{pf}}(s)$ reduce to, for each device i ,

$$D_i^{\text{pf}}(s) \text{ is stable and strictly proper,} \quad (1\text{-i})$$

$$\text{Re}[D_i^{\text{pf}}(j\omega)] > 0, \quad \forall, \omega \in [0, \infty). \quad (1\text{-ii})$$

Voltage control: Strict passivity and the small-gain condition of the loop-shifted qv-dynamics $D^{\text{qv}}(s)(I - \Gamma^{\text{qv}} D^{\text{qv}}(s))^{-1}$ are guaranteed if each device i satisfies

$$D_i^{\text{qv}}(s) \text{ is stable and strictly proper,} \quad (2\text{-i})$$

$$c_i < \text{Re}[D_i^{\text{qv}}(j\omega)^{-1}], \quad \forall, \omega \in [0, \infty). \quad (2\text{-ii})$$

If all devices satisfy conditions (1-i), (1-ii), (2-i), and (2-ii), then the overall interconnection $D \# N$ is internally stable.

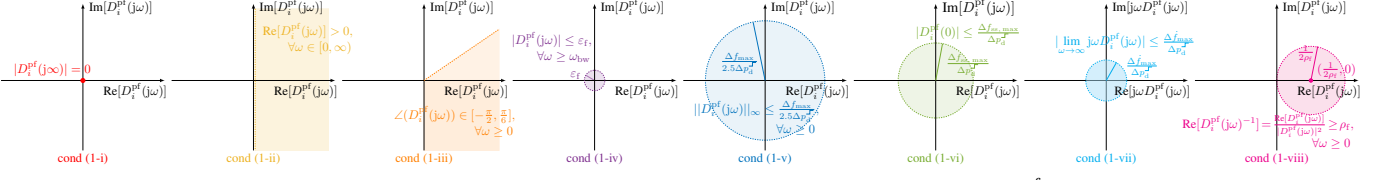


Fig. 3: Qualitative graphical illustration of the eight frequency-domain conditions (1-i) to (1-viii) for each $D_i^{\text{pf}}(j\omega)$ in the complex plane.

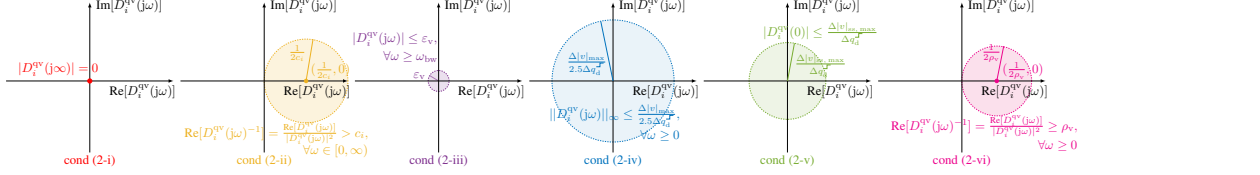


Fig. 4: Qualitative graphical illustration of the six frequency-domain conditions (2-i) to (2-vi) for each $D_i^{\text{qv}}(j\omega)$ in the complex plane.

B. Performance Certification Criteria

We next certify system-wide performance for the average-mode system frequency response of the pf-subsystem, and for local open-loop voltage responses of the qv-subsystem.

Frequency Control: Performance limits are imposed on the average-mode frequency response derived in (6) expressed through time-domain metrics after a worst-case active-power step disturbance $\Delta p_d^{\sum}(s) = \frac{1}{s}\Delta p_d^{\text{f}}$. The considered time-domain metrics include a bounded nadir $\sup_{t \geq 0} |\Delta f_{\text{avg}}^{\text{f}}(t)| \leq \Delta f_{\text{max}}$, a bounded steady-state deviation $|\lim_{t \rightarrow \infty} \Delta f_{\text{avg}}^{\text{f}}(t)| \leq \Delta f_{\text{ss, max}}$, a bounded RoCoF $\sup_{t \geq 0} |\Delta \dot{f}_{\text{avg}}^{\text{f}}(t)| \leq \Delta \dot{f}_{\text{max}}$, and sufficiently damped oscillations, which are ensured if each device satisfies the conditions in (1-i) and (1-ii), and:

$$\begin{aligned} \angle(D_i^{\text{pf}}(j\omega)) &\in [-\frac{\pi}{2}, \frac{\pi}{6}], \quad \forall \omega \geq 0, & (1-\text{iii}) \\ |D_i^{\text{pf}}(j\omega)| &\leq \varepsilon_{\text{f}}, \quad \forall \omega \geq \omega_{\text{bw}}, & (1-\text{iv}) \\ \|D_i^{\text{pf}}(j\omega)\|_{\infty} &\leq \frac{\Delta f_{\text{max}}}{2.5, \Delta p_d^{\text{f}}}, \quad \forall \omega \geq 0, & (1-\text{v}) \\ |D_i^{\text{pf}}(0)| &\leq \frac{\Delta f_{\text{ss, max}}}{\Delta p_d^{\text{f}}}, & (1-\text{vi}) \\ |\lim_{\omega \rightarrow \infty} j\omega D_i^{\text{pf}}(j\omega)| &\leq \frac{\Delta \dot{f}_{\text{max}}}{\Delta p_d^{\text{f}}}, & (1-\text{vii}) \\ \text{Re}[D_i^{\text{pf}}(j\omega)^{-1}] &\geq \rho_{\text{f}}, \quad \forall \omega \geq 0. & (1-\text{viii}) \end{aligned}$$

Here, ω_{bw} is a prescribed bandwidth, $\varepsilon_{\text{f}} \approx 0$ enforces roll-off for $\omega \geq \omega_{\text{bw}}$, and $\rho_{\text{f}} > 0$ is an output feedback passivity index selected to ensure adequate damping. Conditions (1-iii), (1-iv) and (1-v) bound the nadir, (1-vi) bounds the steady-state deviation, (1-vii) bounds RoCoF, and (1-viii) enforces sufficiently damped oscillations. A graphical illustration of the eight frequency-domain conditions (1-i) to (1-viii) for each $D_i^{\text{pf}}(j\omega)$ is provided in Fig. 3. A key technical step is to show that the imposed local conditions guarantee the corresponding properties of the aggregate transfer function $D_{\text{avg}}(s)$, which in turn imply the desired time-domain bounds on the average-mode frequency response. The proof relies on properties of the Fourier integral and related algebraic arguments taken from [13].

Voltage Control: In the qv-subsystem there is no meaningful average mode; instead, voltage deviations are predominantly local. Accordingly, we approximate

$$\Delta|v|_i(s) \approx D_i^{\text{qv}}(s), \Delta q_{d,i}(s), \quad (9)$$

and impose local time-domain bounds on the peak and steady-state voltage deviations, i.e., $\sup_{t \geq 0} |\Delta|v|_i^{\text{f}}(t)| \leq \Delta|v|_{\text{max}}$ and $|\lim_{t \rightarrow \infty} \Delta|v|_i^{\text{f}}(t)| \leq \Delta|v|_{\text{ss, max}}$, together with sufficient damping, under a worst-case reactive-power step $\Delta q_{d,i}(s) =$

$\frac{1}{s} \Delta q_{\text{d}}^{\text{f}}$. These time-domain requirements are guaranteed if each device satisfies the conditions in (2-i) and (2-ii) and:

$$|D_i^{\text{qv}}(j\omega)| \leq \varepsilon_{\text{v}}, \quad \forall \omega \geq \omega_{\text{bw}}, \quad (2-\text{iii})$$

$$\|D_i^{\text{qv}}(j\omega)\|_{\infty} \leq \frac{\Delta|v|_{\text{max}}}{2.5, \Delta q_{\text{d}}^{\text{f}}}, \quad \forall \omega \geq 0, \quad (2-\text{iv})$$

$$|D_i^{\text{qv}}(0)| \leq \frac{\Delta|v|_{\text{ss, max}}}{\Delta q_{\text{d}}^{\text{f}}}, \quad (2-\text{v})$$

$$\text{Re}[D_i^{\text{qv}}(j\omega)^{-1}] \geq \rho_{\text{v}}, \quad \forall \omega \geq 0. \quad (2-\text{vi})$$

Here, $\varepsilon_{\text{v}} \approx 0$ enforces roll-off beyond ω_{bw} , and $\rho_{\text{v}} > 0$ is chosen to ensure adequate damping. A graphical illustration of conditions (2-i) to (2-vi) is provided in Fig. 4. The proof parallels the frequency case, but applies directly to $D_i^{\text{qv}}(s)$.

IV. NEXT GENERATION GRID CODE SPECIFICATIONS

Based on the derived stability and performance conditions, we formulate *Next Generation Grid Code (NGGC)* specifications for frequency and voltage regulation: Each generation unit shall implement its pf- and qv-control via transfer functions $D_i^{\text{pf}}(s)$ and $D_i^{\text{qv}}(s)$ that satisfy the decentralized conditions in (1-i) to (1-viii) and (2-i) to (2-vi), respectively. Compliance with these specifications guarantees closed-loop stability and system-wide performance. The NGGC requirements admit an intuitive graphical interpretation in the complex plane, exemplarily illustrated by the Nyquist-plot envelopes in Fig. 5 for the pf-control (with an analogous interpretation for the qv-control).

V. NUMERICAL EXPERIMENT

To validate the proposed NGGC framework and its stability and performance guarantees, we conduct numerical experiments in MATLAB/Simulink using a simple two-node system with two devices interconnected by an *RL* line. The setup follows the modeling assumptions of the NGGC framework: a quasi-stationary phasor-based network model is used, and only outer-loop device dynamics are implemented, neglecting inner converter loops and fast synchronous-machine dynamics. The numerical studies evaluate established generation-unit controls, including grid-forming VSCs and synchronous generators (SGs), with respect to the proposed NGGC conditions. We focus on the pf-subsystem while fixing all bus voltages at 1 p.u.

In the *first experiment*, one node is equipped with an ideal VSC employing a feasible control $D_1^{\text{pf}}(s)$, while the device under test (DUT) at the second node is varied. The considered DUTs include static droop (DUT 1), virtual oscillator control (VOC) (DUT 2), virtual synchronous machine (VSM) (DUT

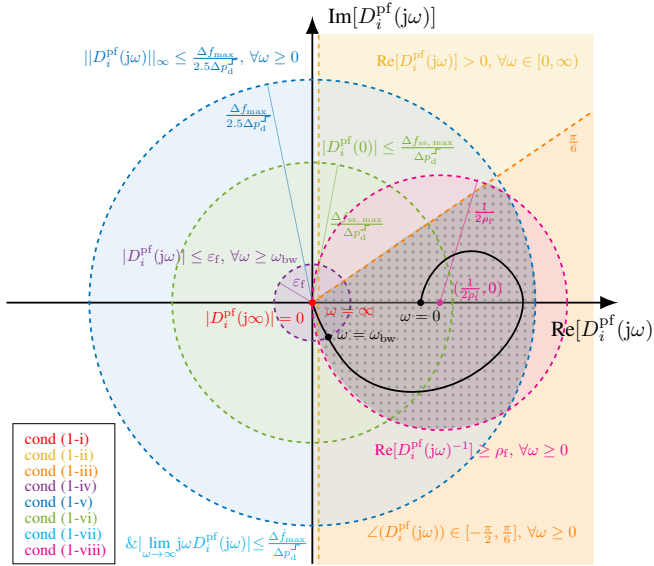


Fig. 5: Superposition of NGGC conditions (1-i) to (1-viii) in Fig. 3. The gray shaded region indicates the feasible set for all $\omega \in (0, \omega_{bw})$, and the black curve depicts an exemplary feasible Nyquist plot of $D_i^pf(j\omega)$.

3), generalized second-order droop control (DUT 4), and SGs with non-reheat steam (DUT 5), reheat steam (DUT 6), and hydro turbines (DUT 7) (parameters from [14]). Their Nyquist characteristics and NGGC compliance are summarized in Fig. 6 and Table I. A 0.1 p.u. active-power load step is applied at the DUT node, and the resulting average-mode frequency responses are shown in Fig. 7a. All configurations remain stable, consistent with approximate satisfaction of the passivity conditions (1-i) and (1-ii). While the steady-state frequency deviation remains within the ENTSO-E limit $\Delta f_{ss,max} = 0.2$ Hz for all DUTs (condition (1-vi) satisfied), the frequency nadir correlates strongly with $\|D_2^pf(s)\|_\infty$. Although SG-based DUTs 5-7 violate condition (1-v), the ideal VSC at node 1 limits the nadir well below the ENTSO-E bound $\Delta f_{max} = 0.8-1$ Hz. RoCoF behavior and oscillation damping are consistent with conditions (1-vii) and (1-viii), respectively, where DUT 1&2 and DUT 4, violating condition (1-vii), exhibit the highest RoCoF, even exceeding the ENTSO-E limit of $\Delta \dot{f}_{max} = 2-2.5$ Hz/s.

In the *second experiment*, both nodes are equipped with identical DUTs. The corresponding frequency responses in Fig. 7b exhibit markedly degraded performance: the nadir exceeds the ENTSO-E limit for DUT 7 (violation of conditions (1-iii) and (1-v)), RoCoF constraints are violated for DUT 1&2 and DUT 4 (violation of condition (1-vii)), and pronounced oscillations appear for SG-based DUTs 5-7 (violation of condition (1-viii)). Overall, these results demonstrate that the proposed NGGC conditions capture key stability and performance trends and provide meaningful guidance for device-level control design.

VI. CONCLUSION

This paper presented preliminary results toward a decentralized, frequency-domain framework for certifying stability and performance in *Next Generation Grid Codes*. The approach provides an initial, model-agnostic basis for linking local device behavior to system-level stability and performance. Ongoing work is extending these findings through larger-scale numerical studies with detailed network and device models, which will also investigate the dynamic behavior of the qv-subsystem.

	(1-i)	(1-ii)	(1-iii)	(1-iv)	(1-v)	(1-vi)	(1-vii)	(1-viii)
DUT 1 & 2	✗	✓	✓	✗	✓	✓	✗	✓
DUT 3	✓	✓	✓	✓	✓	✓	✓	✓
DUT 4	✓	✓	✓	✗	✓	✓	✗	✓
DUT 5	✓	✗	✗	✓	✗	✓	✓	✗
DUT 6	✓	✓	✗	✓	✗	✓	✓	✗
DUT 7	✓	✗	✗	✓	✗	✓	✓	✗

TABLE I: NGGC compliance of the different DUT control laws $D_2^pf(s)$.

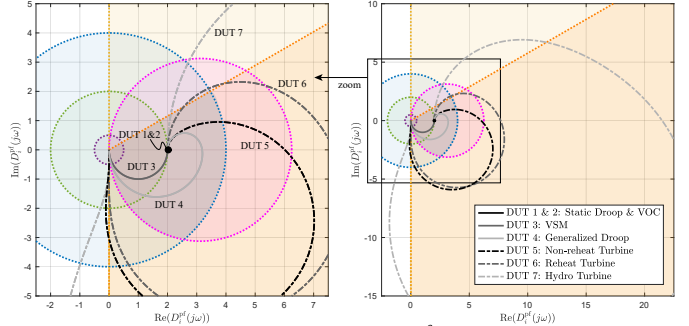


Fig. 6: Nyquist plots of the DUT controllers $D_2^pf(s)$, with NGGC conditions indicated using the same colors as in Fig. 5.

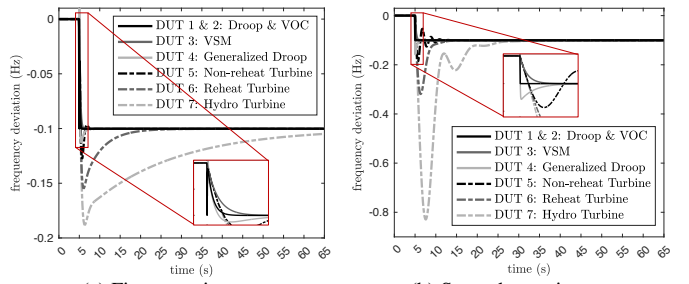


Fig. 7: Average-mode frequency responses of the two-node test system.

REFERENCES

- [1] “Commission regulation (EU) 2016/631 of 14 april 2016, establishing a network code on requirements for grid connection of generators,” tech. rep., European Commission, 2016.
- [2] “The technical requirements and the prequalification process of fast frequency reserve (ffr),” tech. rep., Oyj, Fingrid, 2021.
- [3] “Techn. Anforderungen an Netzbildende Eigenschaften inkl. der Bereitstellung von Momentanreserve,” tech. rep., VDE FNN Hinweis, 2024.
- [4] D. Groß, “Compensating network dynamics in grid-forming control,” in *2022 58th Annual Allerton Conference on Communication, Control, and Computing (Allerton)*, pp. 1–8, 2022.
- [5] H. Geng, X. Xi, and G. Yang, “Small-signal stability of power system integrated with ancillary-controlled large-scale DFIG-based wind farm,” *IET Renewable Power Generation*, vol. 11, no. 8, pp. 1191–1198, 2017.
- [6] “Technical requirements for frequency containment reserve provision in the nordic synchronous area,” tech. rep., ENTSO-E, 2022.
- [7] A. Hoke *et al.*, “White paper: Grid forming functional specifications for bps-connected battery energy storage systems,” tech. rep., North American Electric Reliability Corporation (NERC), 2023.
- [8] Z. Siahaan, E. Mallada, and S. Geng, “Decentralized stability criteria for grid-forming control in inverter-based power systems,” in *2024 IEEE Power & Energy Society General Meeting*, pp. 1–5, IEEE, 2024.
- [9] V. Häberle, X. He, L. Huang, F. Dörfler, and S. Low, “Decentralized parametric stability certificates for grid-forming converter control,” *arXiv preprint arXiv:2503.05403*, 2025.
- [10] L. Huang, D. Wang, X. Wang, H. Xin, P. Ju, K. H. Johansson, and F. Dörfler, “Gain and phase: Decentralized stability conditions for power electronics-dominated power systems,” 2024.
- [11] L. Huang, L. Luo, R. Leng, H. Xin, D. Wang, and F. Dörfler, “Geometric decentralized stability condition for power systems based on projecting dw shells,” *arXiv:2508.17033*, 2025.
- [12] Y. Jiang, A. Bernstein, P. Vorobev, and E. Mallada, “Grid-forming frequency shaping control for low-inertia power systems,” in *2021 American Control Conference (ACC)*, pp. 4184–4189, 2021.
- [13] A. Papoulis, *The Fourier Integral and its Applications*. McGraw-Hill, New York, 1962.
- [14] P. Kundur, *Power System Stability and Control*. McGraw-Hill, 1994.